Inorganic Chemistry

pubs.acs.org/IC
Article

Structure and Spin-Glass Magnetism of the $Fe_{1.5}Ni_{1.5}Ga_4$ Metallic Alloy

Krishnendu Buxi, Rahul Pan, Zvonko Jagličić, Andreja Jelen, Jože Luzar, Peter Mihor, Stanislav Vrtnik, Primož Koželj, Julia Petrović, Maxim Avdeev, Partha Pratim Jana,* and Janez Dolinšek*

Cite This: https://doi.org/10.1021/acs.inorgchem.5c05447

ABSTRACT: The Ga-rich region of the Fe−Ni−Ga ternary system was investigated, by exploring a line of compositions $Fe_xNi_{3-x}Ga_4$, with $0.5 \leq x \leq 2.5$. The single-phase cubic material was found only at the composition $Fe_{1.5}Ni_{1.5}Ga_4$ and its immediate vicinity, representing a new phase in the Fe−Ni−Ga diagram. The homogeneity range of this phase was estimated by additionally exploring a set of compositions $Fe_xNi_yGa_z$ around the central composition $Fe_{1.5}Ni_{1.5}Ga_4$. The structural model was constructed based on the structure of the binary Ni_3Ga_4 parent phase, which crystallizes in the cubic $Ia\bar{3}d$ space group. We have considered that by substituting Fe for Ni, the $Ia\bar{3}d$ structure is preserved, with the Fe and Ni being statistically distributed at their 48*g* Wyckoff site. The possibility of a symmetry-reduced chiral structural model $I4_132$ driven by chemical ordering of Fe and Ni cannot be entirely ruled out on the basis of the crystallographic study. The magnetic study of the $Fe_{1.5}Ni_{1.5}Ga_4$ phase has revealed that the material forms a spin glass phase below the spin freezing temperature $T_f \approx 9$ K. Since the spin glass ordering of the Fe and Ni magnetic moments is compatible with their random distribution, the magnetic study supports the disordered cubic $Ia\bar{3}d$ model.

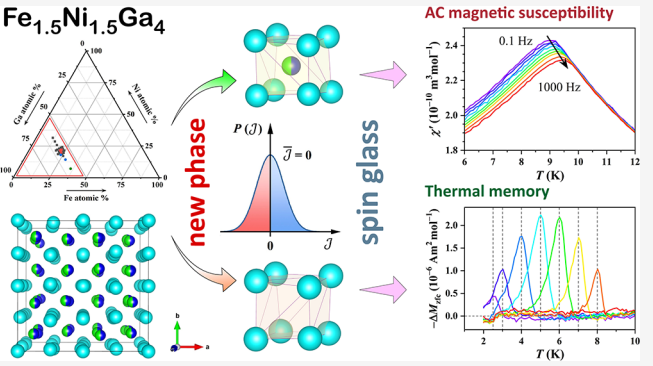

1. INTRODUCTION

Intermetallic compounds of transition metals with gallium (Ga) are well-known for their diverse structural variations and interesting physical/chemical properties. The group of gallides includes compounds with TiNiSi-type structure (ScNiGa, ScPtGa, ScAuGa), ZrBeSi-type NbRhGa, $MgZn_2$-type $NbCr_{1.58}Ga_{0.42}$ and $NbFe_{1.51}Ga_{0.49}$,[1] $Ti_{2-x}Ni_3Ga_9$ ternary intermetallics with a distorted $HoCoGa_5$-type structure,[2] various gallium-based Heusler alloys of the type X_2ZGa, with X and Z standing for 3*d* transition metals, including ferromagnetic Co_2ZGa series,[3] superconducting $ReGa_5$,[4] magnetic α-Fe_6Ga_5 and GaMn,[5,6] magnetocaloric $MnNiGa_2$ full-Heusler alloy[7] and other magnetocaloric alloys in the Ni−Mn−Ga system[8−11] and thermoelectric Fe_2CoGa Heusler alloy.[12] Bimetallic compounds of Ga with transition metals show superior catalytic properties in heterogeneous catalysis. The Pd_mGa_n series (PdGa, Pd_2Ga, Pd_3Ga_7) are highly selective and stable catalyst materials for the selective hydrogenation of alkynes and the methanol steam reforming reaction,[13−16] while noble metal-free intermetallic compounds in the Ni−Ga system (NiGa, Ni_2Ga_3, Ni_3Ga, Ni_5Ga_3) were reported to reduce CO_2 to methanol at ambient pressure.[17−19]

Recently, a novel chiral intermetallic compound $Co_3Ni_3Ga_8$ was reported,[20] obtained by substituting half of the Ni atoms by Co in the binary parent compound Ni_3Ga_4 ($Ia\bar{3}d$, *c*I112).[21,22] The substitution induces local distortions in the lattice, driven by chemical ordering of Ni and Co, which makes the $Co_3Ni_3Ga_8$ compound to adopt a lower-symmetric chiral structure $I4_132$, as compared to the parent Ni_3Ga_4. The report[20] also provides a theoretical prediction of antiferromagnetic spin ordering in both the binary Ni_3Ga_4 and its ternary derivative $Co_3Ni_3Ga_8$. An interesting feature emerges in the electron density of states diagrams. As the number of electrons in the $Co_3Ni_3Ga_8$ is reduced with respect to the binary Ni_3Ga_4, the *d*-band of the transition metal atoms shifts closer to the Fermi level.[20] These results motivated us to investigate the Fe substitution for Ni in the Ni_3Ga_4 for two reasons: (1) Fe, due to its slightly larger atomic-size mismatch relative to Ni may induce larger local distortions than Co, potentially leading to interesting structural transformations and (2) Fe substitution further reduces the electron count of the system, which may shift the *d*-band of the transition metals

Received: November 19, 2025
Revised: January 14, 2026
Accepted: February 18, 2026
Published: February 20, 2026

closer to the Fermi level, opening the door to novel magnetic and transport properties.

According to the Fe−Ni−Ga ternary phase diagram,[23] the Ga-poor region contains at least two intermetallic phases, the Heusler alloy Fe_2NiGa ($Fm\bar{3}m$, $cF16$)[24] and the monoclinic $FeNi_2Ga$ ($C2/m$, $mS40$).[25] These compounds were identified as ferromagnetic shape memory alloys.[26] The Ga-rich part of the ternary system remains largely unexplored. In this course of investigation, the Ga-rich region of the Fe−Ni−Ga ternary system is explored by studying a line of compositions at a constant Ga content $Fe_xNi_{3-x}Ga_4$, with $0.5 \leq x \leq 2.5$. Single-phase material was found only at the composition $Fe_{1.5}Ni_{1.5}Ga_4$ and its immediate vicinity. The existence range of the $Fe_{1.5}Ni_{1.5}Ga_4$ phase was estimated by additionally exploring a set of compositions $Fe_xNi_yGa_z$, where the concentrations of all three elements were varied independently around the central composition $Fe_{1.5}Ni_{1.5}Ga_4$. We are reporting on the crystal structure and magnetic properties of the cubic $Fe_{1.5}Ni_{1.5}Ga_4$ phase, representing a new phase in the Fe−Ni−Ga ternary system. The structural model is constructed based on the structure of binary Ni_3Ga_4.[21,22] Like the binary Ni_3Ga_4, the structure is considered to crystallize in the cubic $Ia\bar{3}d$ space group, where Fe substitutes Ni to form $Fe_{1.5}Ni_{1.5}Ga_4$. Here it is noteworthy that, though the Fe_3Ga_4 in the Fe−Ga system[27−29] has a similar composition to Ni_3Ga_4, it adopts a monoclinic structure ($C2/m$, $mS42$). A ferrimagnetic ordering in the low Ni-doped solid solution of the Fe_3Ga_4 has been reported.[30] The possibility of a symmetry-reduced chiral structural model $I4_132$ of the $Fe_{1.5}Ni_{1.5}Ga_4$ phase, driven by chemical ordering between Fe and Ni cannot be entirely ruled out on the basis of the crystallographic study, because of the weak X-ray scattering contrast between Fe and Ni and their similar neutron coherent scattering lengths. The magnetic study, on the other hand, supports the $Ia\bar{3}d$ structural model without chemical ordering of Fe and Ni, because the $Fe_{1.5}Ni_{1.5}Ga_4$ phase behaves magnetically at low temperatures as a spin glass, compatible with statistical distribution of the Fe and Ni atomic magnetic moments in a single Wyckoff site.

2. MATERIAL SYNTHESIS AND STRUCTURAL CHARACTERIZATION

2.1. Synthesis

Ten $Fe_xNi_{3-x}Ga_4$ compositions with nominal Fe contents x = 0.5, 0.8, 1.0, 1.2, 1.4, 1.5, 1.6, 1.8, 2.0, and 2.5, as well as 14 compositions $Fe_xNi_yGa_z$ with $1.3 \leq x \leq 1.74$, $1.26 \leq y \leq 1.7$ and $3.8 \leq z \leq 4.2$ were synthesized from pure constituent elements nickel powder (99.995%), gallium metal (99.9%) and iron granules (1−2 mm, 99.98%), all from Alfa Aesar, using high-temperature synthesis technique. Given that gallium metal remains liquid at room temperature (RT), handling requires additional precautions. Gallium was solidified over ice and promptly transferred into a one-end-sealed silica tube of diameter ∼ 8 mm. Nickel powder and iron granules were weighted and transferred. The tubes were connected to a vacuum sealing unit, and pure argon gas was purged into the evacuated tubes multiple times to remove the trace amount of air. Then the samples were sealed in vacuum (∼10^{-6} mbar) to avoid metal oxide formation at elevated temperatures. The sealed tubes were placed into a cylindrical alumina crucible covered with sand-sized quartz clasts to buffer against the temperature fluctuations during heat treatment. The alumina crucibles were placed into a muffle furnace, which was ramped up to 1223 K at a rate of 62 Kh^{-1} and held at that temperature for 17 h, followed by cooling to 723 K at a rate of 9 Kh^{-1}. The samples were dwelled at that temperature for a prolonged time (∼8−9 days). Then the samples were cooled to 473 K at a rate of 4 Kh^{-1}, and at this stage the furnace was turned off and allowed to cool to ambient temperature. The large-scale samples (4 g for neutron powder diffraction) were prepared in an ampule of a diameter ∼ 12 mm, using longer annealing time (∼9−10 days) at 723 K. The ingots obtained after the reactions were air-stable with a shiny metallic luster. The ingots were broken with an agate mortar and pestle into small crystallites, which were then used for further characterization.

2.2. Structure Solution and Refinement by Single-Crystal X-ray Diffraction

The single-crystal X-ray diffraction (SCXRD) data collection and processing are detailed in the Experimental section. The data collected for the $Fe_{1.5}Ni_{1.5}Ga_4$ crystal were indexed based on a = 11.5192 Å cubic I-centered unit cell and the $hk0$ and hhl planes in the reciprocal space are shown in Figure S1 of the Supporting Information. The extinction conditions in the reciprocal space suggested the space group $Ia\bar{3}d$ (No. 230). The charge flipping algorithm[31] in JANA2006[32] yielded three independent crystallographic sites, 16a, 48f, and 48g, among which 16a and 48f were occupied by Ga, and 48g was occupied by Fe. The refinement converged to R_{obs} ∼ 0.048. An independent refinement of the Fe position resulted in the site occupancy factor (SOF) greater than unity; therefore, this site was examined for Ni occupancy and subsequent refinement resulted in SOF (Ni) less than one. Hence, the 48g site was modeled as statistically mixed between Fe and Ni, and the SOF was fixed according to the nominal composition, assuming complete occupancy at that site. The refinement at this stage resulted in R_{obs} ∼ 0.040. In the next step, the atomic sites were refined anisotropically, and the refinement applying isotropic extinction correction yielded R_{obs} ∼ 0.017 and goodness-of-fit (GOF) of 1.33. No significant electron density was found on the difference Fourier map. The X-ray crystallographic data on the structure solution and refinement are detailed in Table 1, while the atomic coordinates, site occupancies and isotropic displacement parameters are given in Table 2. The structural data are also available as a CIF file, deposited in the Cambridge Crystallographic Data Centre (CCDC) as the number CSD 2502085.

2.3. EDS and Elemental Mapping Analysis

Energy dispersive X-ray spectroscopy (EDS) compositional point analysis averaged over ten points yielded the composition (in at %, rounded to first integers) $Fe_{20}Ni_{22}Ga_{58}$, with about ±0.5 at. % uncertainty for each element, in good agreement with the loading composition $Fe_{21.43}Ni_{21.43}Ga_{57.14}$ of the $Fe_{1.5}Ni_{1.5}Ga_4$ phase. EDS elemental maps of a larger piece of material show homogeneous distribution of the elements on a 100-μm scale (Figure S2).

2.4. Neutron Powder Diffraction Analysis

Due to the very weak X-ray scattering contrasts between Fe, Ni and Ga elements, an accurate distribution of the atoms cannot be determined based on the electron density only. Hence, a combination of X-ray and neutron powder diffraction (NPD) experiments was employed to overcome this problem. NPD allows accurate determination of the Ga site as the neutron coherent scattering length b of Ga (b_{Ga} = 7.288 fm) is distant enough from Fe (b_{Fe} = 9.45 fm) and Ni (b_{Ni} = 10.3 fm), whereas the site occupancy pattern of Fe and Ni cannot be reliably determined due to their too similar neutron coherent scattering lengths. The intensity of additional diffraction peaks due to complete Fe and Ni ordering and the splitting of the original Wyckoff site 48g in the $Ia\bar{3}d$ space group into 24h and 24g sites in the $I4_132$ would be on the scale of 0.8% of the strongest peak, which is below the detection level for the collected data. The Rietveld refinement of the NPD data at RT for the $Ia\bar{3}d$ model using JANA2006 software[32] is shown in Figure 1a (the refinement parameters are given in the figure caption).

The analysis supports the cubic $Ia\bar{3}d$ model, but is still inconclusive with regard to the possible chemical ordering of Fe and Ni, which could lead to the symmetry-reduced chiral structural model $I4_132$. A comparison of the NPD data collected at 3 and 300 K is shown in Figure 1b. No new (magnetic) peaks or intensity enhancements at low 2θ angles could be detected at 3 K in addition to the nuclear

https://doi.org/10.1021/acs.inorgchem.5c05447
Inorg. Chem. XXXX, XXX, XXX−XXX

Table 1. Crystallographic Data Collection and Refinement for the $Fe_{1.5}Ni_{1.5}Ga_4$ Single Crystal (CSD Deposition Number 2502085)

crystallographic data	
chemical formula	$Fe_{1.5}Ni_{1.5}Ga_4$
chemical formula (at.%)	$Fe_{21.43}Ni_{21.43}Ga_{57.14}$
EDS formula (at.%)	$Fe_{19.5}Ni_{22.2}Ga_{58.3}$
crystal system	cubic
space group; Z	$Ia\bar{3}d$ (No. 230); 16
a/Å	11.5192(4)
V/Å^3	1528.51(9)
ρ_{calc}/g cm^{-3}	7.8339
μ/mm^{-1}	40.29
$F(000)$	3280
crystal color	silvery with metallic luster
data collection	four-circle diffractometer
diffractometer	Bruker Photon II
radiation; wavelength/Å	Mo Kα; 0.71073
monochromator	graphite
T/K	294(2)
$\theta_{min} - \theta_{max}$/deg	4.33−36.17
reflns measured	18,460
index range	$-19 \le h \le 19$
	$-19 \le k \le 19$
	$-19 \le l \le 19$
data reduction/abs. correction	multiscan
crystal size/mm	0.09 × 0.07 × 0.02
unique reflns	312
R_{int}	0.0551
structure solution/refinement	JANA2006 package program
structure solution	superflip
no. reflns used	4626
no. variables	14
observed reflns ($I > 3\sigma(I)$)	259
$R(F^2 > 3\sigma(F^2))$	0.0171
$R(F)$ (all data)	0.0231
$wR(F^2)$ (all data)	0.0453
GOF (all)	1.33
$\Delta\rho_{min}/\Delta\rho_{max}$ (eÅ^{-3})	−0.75/0.51

peaks, indicating the absence of long-range magnetic ordering down to that temperature. The variation of the peak intensity at higher 2θ angles for the 3 K data compared to the 300 K data can be attributed to the Debye−Waller factor.[33]

2.5. Phase Analysis by Powder X-ray Diffraction

The phase width has been analyzed by powder X-ray diffraction (PXRD) study. The PXRD data refinements (Rietveld and Le Bail) were performed employing JANA2006 software.[32] The Rietveld refinement diffractogram for the $Fe_{1.5}Ni_{1.5}Ga_4$ is depicted in Figure 2, while the diffractograms of the refinements (Rietveld or Le Bail) for other synthesized samples in the $Fe_xNi_{3-x}Ga_4$ series are given in Figure S3 of the Supporting Information (the refinement parameters are detailed in Table S1). Single-phase material with the $Ia\bar{3}d$ structure (and generic phase name $Fe_{1.5}Ni_{1.5}Ga_4$) was found only for the compositions $x = 1.5$ and 1.6 (corresponding to $Fe_{21.43}Ni_{21.43}Ga_{57.14}$ and $Fe_{22.86}Ni_{20.00}Ga_{57.14}$, in at.%), while at other compositions, two to four phases were present (Table S1). For the compositions $0.8 \le x \le 1.8$, the major phase was the cubic $Ia\bar{3}d$, whereas for $x = 2.0$ and 2.5, the major phase was monoclinic $C2/m$.

The refined PXRD diffractograms of the 14 $Fe_xNi_yGa_z$ samples are shown in Figure S4, whereas the refinement parameters are given in Table S2 of the Supporting Information. For this series, single-phase cubic $Ia\bar{3}d$ material was found only at the composition $Fe_{22.06}Ni_{22.06}Ga_{55.88}$ (i.e., $Fe_{1.5}Ni_{1.5}Ga_{3.8}$), while for other compositions, two to four phases were present (Table S2), with the $Ia\bar{3}d$ being the major phase for all compositions except one (the $Fe_{23.54}Ni_{18.01}Ga_{58.45}$ or $Fe_{1.65}Ni_{1.26}Ga_{4.09}$). For that particular composition, the major phase was the monoclinic $C2/m$, while the $Ia\bar{3}d$ phase was not detected.

The phase analysis discerns that the cubic $Ia\bar{3}d$ phase exists as a single phase only in a narrow homogeneity range around the $Fe_{1.5}Ni_{1.5}Ga_4$ composition, shown in the Fe−Ni−Ga ternary phase triangle of Figure 3. Other investigated compositions are multiphase (from two up to four phases), where the cubic $Ia\bar{3}d$ is the major phase for most compositions. The exceptions are the compositions $Fe_{28.57}Ni_{14.29}Ga_{57.14}$ (Fe_2NiGa_4) and $Fe_{23.54}Ni_{18.01}Ga_{58.45}$ ($Fe_{1.65}Ni_{1.26}Ga_{4.09}$), where the major phase is the monoclinic $C2/m$, whereas the composition $Fe_{35.71}Ni_{7.14}Ga_{57.14}$ ($Fe_{2.5}Ni_{0.5}Ga_4$) is a single-phase $C2/m$.

2.6. $Fe_{1.5}Ni_{1.5}Ga_4$ Structure Description

The parent compound Ni_3Ga_4 ($Ia\bar{3}d$, a = 11.411 Å) (Figure 4a) can be described as a 3D-network of face-sharing Ga_8 cubes extending along the crystallographic axes, where 3/4 of the cubic voids are occupied by Ni (Figure 4b) (Ni@Ga8) and the remaining 1/4 of them remain vacant (V@Ga8) (Figure 4c).[21,22] Therefore, Ni_3Ga_4 can be considered as a *lacunar* CsCl-type phase. The volumes of the occupied and vacant Ga_8 cubes are equal ($V_{Ni\ @\ Ga8} = V_{V\ @\ Ga8}$= 23.61 Å^3). Consequently, each Ni atom is surrounded by four other Ni atoms within the bonding distances (~2.85 Å) (Figure 4d).

This arrangement can be correlated with the electronic stability of this compound, which adheres to the 18-n rule to achieve a closed shell electronic configuration, where n represents the number of electron pairs that the atom shares with its neighboring transition metal atoms,[34] and in this case n = 4. Upon replacing half of the Ni atoms with Fe, the unit cell parameter of the $Fe_{1.5}Ni_{1.5}Ga_4$ increases, and certain distortions are introduced into the system without breaking any symmetry element (Figure 4e). As a result, the "filled cubane" expands in volume, $V_{Ni/Fe\ @\ Ga8}$= 25.24 Å^3 (Figure 4f), whereas the "empty cubane" contracts, $V_{V\ @\ Ga8}$ = 22.50 Å^3 (Figure 4g), driven by a reduction in the (Ni/Fe)−(Ni/Fe) bond lengths (~2.78 Å) (Figure 4h) relative to the Ni−Ni bonds in the parent phase. The 18-n rule also breaks down, as achieving the closed-cell electronic configuration for the $Fe_{1.5}Ni_{1.5}Ga_4$ would require each Ni/Fe atom to share 5 electron pairs with the neighboring atoms, i.e., to have five Ni/Fe neighbors within the bonding distances, which is clearly not the case.

3. SPIN GLASS MAGNETISM OF THE $Fe_{1.5}Ni_{1.5}Ga_4$ COMPOUND

Magnetic properties of an $Fe_{1.5}Ni_{1.5}Ga_4$ polycrystalline sample were determined in the temperature interval between 300 and

Table 2. Atomic Coordinates, Site Occupancy Factors (SOF), and Equivalent Isotropic Displacement Parameters for the $Fe_{1.5}Ni_{1.5}Ga_4$ Single Crystal

atom	Wyckoff	x	y	z	SOF	$^*U_{eq}$ /Å^2
Ga1	16a	0	0	0	1	0.00852(6)
Ga2	48f	1/4	0.01408(3)	0	1	0.00866(7)
Ni1/Fe1	48g	0.63462(2)	0.38462(2)	3/8	0.5/0.5	0.00816(7)

$^*U_{eq}$/Å^2 is defined as one-third of the trace of the orthogonalized U^{ij} tensor.

https://doi.org/10.1021/acs.inorgchem.5c05447
Inorg. Chem. XXXX, XXX, XXX−XXX

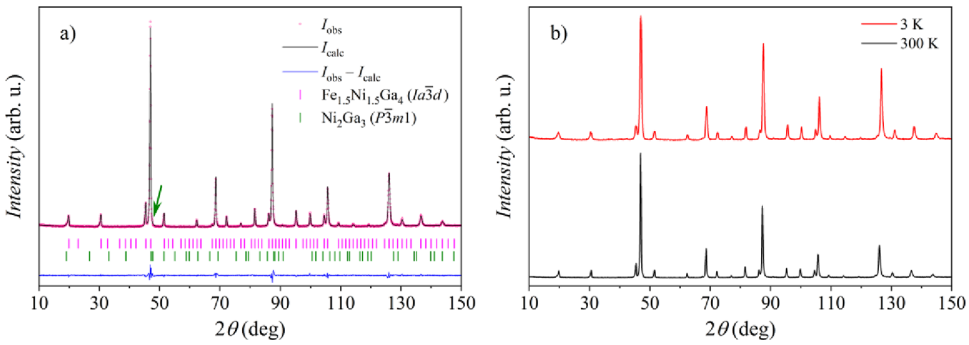

Figure 1. (a) Rietveld refinement of the $Fe_{1.5}Ni_{1.5}Ga_4$ NPD data collected at 300 K (R_{obs} = 0.0244, wR_{obs} = 0.0297, R_p = 0.0484, wR_p = 0.0622, GOF = 1.49). I_{obs} is the observed intensity, I_{calc} the calculated intensity, and $I_{obs} - I_{calc}$ is their difference. Since the large-scale synthesis of the $Fe_{1.5}Ni_{1.5}Ga_4$ material for the NPD study has yielded a trace amount of Ni_2Ga_3 as an impurity phase (its most intense peak is marked by an arrow), the Rietveld refinement was performed by taking into account both $Fe_{1.5}Ni_{1.5}Ga_4$ ($Ia\bar{3}d$) and Ni_2Ga_3 ($P\bar{3}m1$) phases and their weight fractions were determined to be about ∼99 and ∼1 wt %. Bragg positions of both phases are shown by tick marks. (b) A comparison of the NPD data collected at 3 and 300 K temperatures.

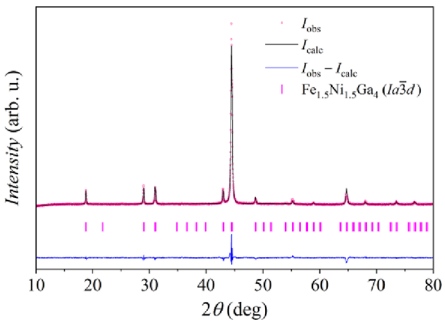

Figure 2. Rietveld refinement diffractogram of the PXRD pattern of $Fe_{1.5}Ni_{1.5}Ga_4$ (R_{obs} = 0.0889, wR_{obs} = 0.1023, R_p = 0.0189, wR_p = 0.0292, GOF = 1.88). Bragg positions of the $Fe_{1.5}Ni_{1.5}Ga_4$ ($Ia\bar{3}d$) phase are shown by tick marks.

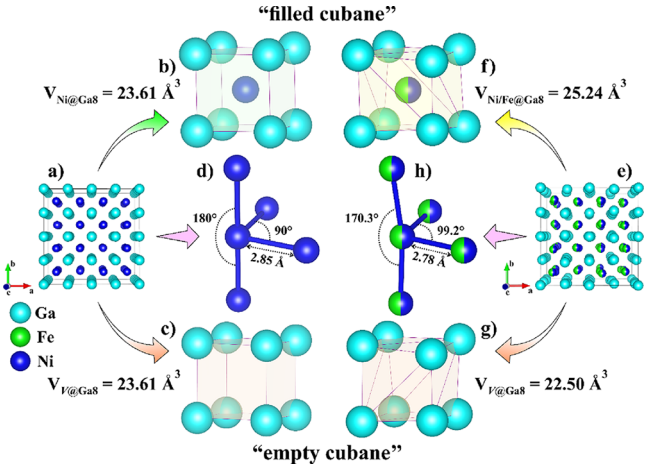

Figure 4. Structural description of (a−d) Ni_3Ga_4 and (e−h) $Fe_{1.5}Ni_{1.5}Ga_4$ (for details, see the text).

1.8 K in magnetic fields up to 7 T, including low magnetic fields of the order 0.1−1 mT. The $Fe_{1.5}Ni_{1.5}Ga_4$ compound contains two magnetic elements, Fe and Ni, both ferromagnetic (FM) as the elemental metals and both occupying the same Wyckoff site in the crystal structure. Since the compound is an electrical conductor, the interspin interaction is the Ruderman−Kittel−Kasuya−Yosida (RKKY) indirect exchange, mediated by the conduction electrons. This long-range interaction oscillates in sign between positive and negative with the interspin distance on the nanometric scale, and consequently there exist both FM and antiferromagnetic (AFM) interactions in the spin system. If the Fe and Ni moments would be randomly distributed over their crystallographic site, magnetic frustration of the spin system without long-range magnetic ordering can be expected, while in the

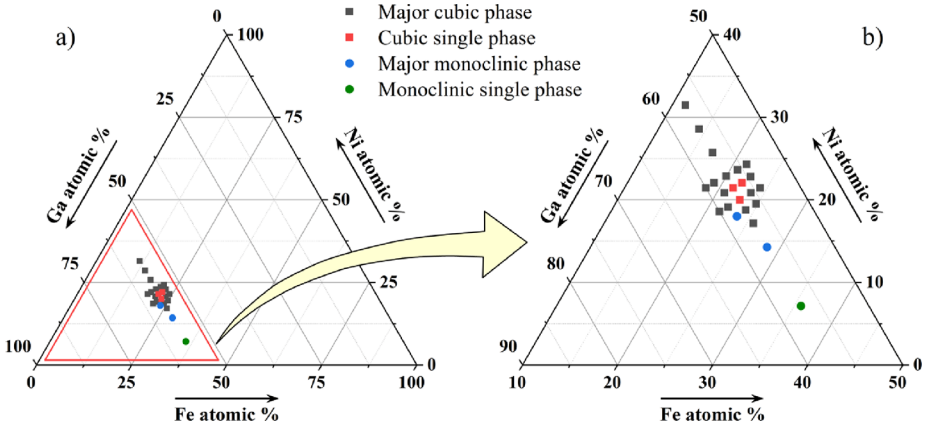

Figure 3. (a) Fe−Ni−Ga ternary phase triangle. (b) Ga-rich portion of the phase triangle magnified, with various symbols denoting the investigated compositions (the legend is written in the figure). Red squares denote the single-phase cubic $Ia\bar{3}d$ compositions.

https://doi.org/10.1021/acs.inorgchem.5c05447
Inorg. Chem. XXXX, XXX, XXX−XXX

case that Fe and Ni would be chemically ordered, the magnetic state could be long-range ordered. All magnetic results presented in the following that are given in units per mol were calculated per mole of $Fe_{0.214}Ni_{0.214}Ga_{0.572}$ "average atoms" with the molar mass of 64.4 g mol^{-1}.

3.1. Temperature-Dependent dc and ac Magnetic Susceptibility

Direct-current (dc) magnetic susceptibility $\chi = M/H$ was determined for both zero-field-cooled (zfc) and field-cooled (fc) protocols. The χ_{zfc} and χ_{fc} susceptibilities in the magnetic field $\mu_0 H = 0.1$ T in the entire investigated temperature range 300−1.8 K are shown in Figure 5, whereas the susceptibilities in various magnetic fields between 0.1 mT and 1 T on an expanded temperature scale below 20 K are shown in the inset.

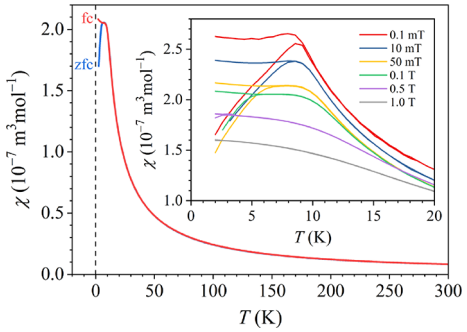

Figure 5. Zfc and fc dc magnetic susceptibilities, χ_{zfc} and χ_{fc}, in the temperature interval 300−1.8 K in the magnetic field $\mu_0 H = 0.1$ T. The inset shows the susceptibilities in various magnetic fields 0.1 mT−1 T on an expanded temperature scale below 20 K.

Upon cooling from RT, the susceptibilities exhibit a $1/T$ Curie-type paramagnetic growth down to about 9 K, with no difference between χ_{zfc} and χ_{fc}. At 9 K, χ_{zfc} exhibits a cusp and decreases toward zero upon further cooling, while χ_{fc} remains constant. These features are characteristic of a spin-freezing transition in a spin glass (SG).[35] The spin-freezing temperature T_f is conveniently defined as the temperature of the χ_{zfc} maximum. Below T_f, spin fluctuation times become macroscopically long and can no longer drive the spin system to thermal equilibrium on the available experimental time scale, so that the system becomes nonergodic. Broken ergodicity is the origin of the $\chi_{zfc} - \chi_{fc}$ splitting.

The strength of the exchange interaction responsible for the formation of the SG magnetic structure was estimated by analyzing the shift of the $\chi_{fc} - \chi_{zfc}$ bifurcation temperature (that equals T_f in the lowest field) to lower temperatures with increasing magnetic field. A continuous shift of the bifurcation temperature with the field is observed (inset in Figure 5), where in the field of 0.5 T, a tiny $\chi_{fc} - \chi_{zfc}$ splitting is still observed at the lowest temperature of 1.8 K, while there is no more difference between χ_{zfc} and χ_{fc} in a 1 T field. This signals that the Zeeman (single-spin) interaction dominates over the exchange (two-spin) interaction and polarizes the spins along the magnetic field direction, whereas the frustrated magnetic structure that has been formed in zero field is destroyed.

The susceptibility in the paramagnetic regime (at $T > T_f \approx 9$ K) was analyzed by the Curie−Weiss law, $\chi = \chi_0 + C/(T - \theta)$, pertinent to an ensemble of localized paramagnetic moments. Here C is the Curie−Weiss constant, θ is the Curie−Weiss temperature and χ_0 is the temperature-independent term (a sum of the negative Larmor diamagnetic susceptibility χ_{Larmor} of the atomic cores, the negative Landau diamagnetic susceptibility χ_{Landau} due to the conduction-electron circulation in an external magnetic field and the positive Pauli spin susceptibility χ_{Pauli} of the conduction electrons, where in the independent-electron model, all three contributions are of the same order of magnitude). The susceptibility in a 0.1 T field is shown in Figure 6 in a $(\chi - \chi_0)^{-1}$ vs T plot. The Curie−Weiss

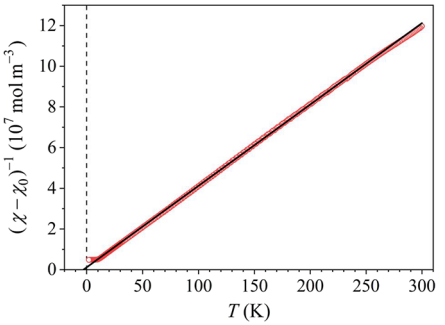

Figure 6. Magnetic susceptibility χ_{fc} in the field $\mu_0 H = 0.1$ T presented in a $(\chi - \chi_0)^{-1}$ vs T plot. The solid line is the Curie−Weiss paramagnetic fit at temperatures $T > 100$ K (the values of the fit parameters are given in the text).

fit performed in the high-temperature regime for $T > 100$ K is shown by a solid line and the fit parameters are $C = 2.5 \times 10^{-6}$ m^3 $Kmol^{-1}$, $\theta = -2.9$ K and $\chi_0 = -1.3 \times 10^{-10}$ m^3 mol^{-1}.

The Curie−Weiss constant allows determination of the mean effective paramagnetic moment $\overline{\mu}_{eff} = \overline{p}_{eff}\mu_B$ (where μ_B is the Bohr magneton and $\overline{p}_{eff}$ is the mean effective Bohr magneton number) from the formula $\overline{p}_{eff} = (797.7\sqrt{mol/m^3K})\sqrt{C}$,[36] yielding $\overline{\mu}_{eff} = 1.93$ μ_B per one $Fe_{0.5}Ni_{0.5}$ "average" magnetic atom. This value is significantly reduced relative to the experimental paramagnetic free-ion values of the localized ions Fe^{3+}, Fe^{2+}, Ni^{3+}, and Ni^{2+} that amount to 5.9, 5.4, 4.8, and 3.2 μ_B, respectively. Such reduction is typical for electrically conducting paramagnets and originates from partial screening of the localized moments by the spins of conduction electrons. The fit-determined χ_0 value was compared to the theoretical Larmor core susceptibility that was calculated from literature tables[37] for different ionization states of the Fe and Ni elements to be in the interval $\chi_{Larmor} = [-1.3, -0.9] \times 10^{-10}$ m^3 mol^{-1}, confirming that χ_0 is of correct order of magnitude. The fact that χ_0 is negative indicates dominance of the two diamagnetic contributions (Larmor and Landau) over the Pauli paramagnetic spin susceptibility.

The Curie−Weiss temperature θ is an indication of the dominant type of interspin interactions, being either FM ($\theta > 0$) or AFM ($\theta < 0$). In 3d magnetic alloys containing randomness, random local magnetic anisotropy at the atomic scale is generally insufficient to pin the local magnetization direction, so that the alloys are exchange-dominated spin systems. Randomness introduces a continuous distribution $P(\mathcal{J})$ of the exchange coupling constants $\mathcal{J}$, which extends on both $\mathcal{J} > 0$ (FM coupling) and $\mathcal{J} < 0$ (AFM coupling) sides of the $\mathcal{J}$ axis.[38] A SG-type $P(\mathcal{J})$ is, by definition, characterized by a zero average exchange interaction, $\overline{\mathcal{J}} = 0$ and consequently θ value close to zero. The negative $\theta = -2.9$ K value of the Curie−Weiss temperature suggests dominant AFM-type interactions, but is small enough to support the SG-

https://doi.org/10.1021/acs.inorgchem.5c05447
Inorg. Chem. XXXX, XXX, XXX−XXX

type magnetic state below $T_f \approx 9$ K, where the FM and AFM interactions are both present in similar proportions.

Alternating-current (ac) susceptibility was measured in a sinusoidal magnetic field of amplitude $\mu_0 H = 0.2$ mT at logarithmically spaced frequencies in the interval $\nu = 0.1$ Hz−1 kHz. The temperature-dependent real part of the susceptibility χ' in the region of the spin-freezing transition is shown in Figure 7. χ' exhibits a peak at T_f, which shifts to higher

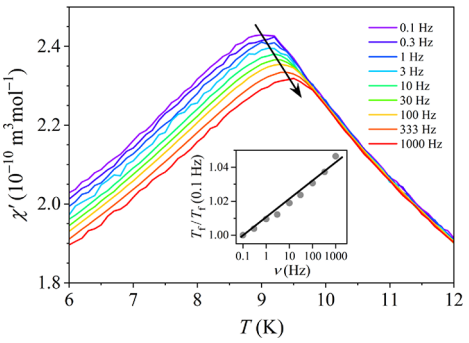

Figure 7. Real part χ' of the ac magnetic susceptibility at frequencies in the interval $\nu = 0.1$ Hz−1 kHz in the temperature range of the spin-freezing transition. The inset shows the $T_f(\nu)/T_f(0.1\ \text{Hz})$ relation on the logarithmic frequency scale.

temperatures with increasing frequency and the peak height slightly decreases. Such behavior is characteristic for a transition to a nonergodic spin state and the temperature of the χ' peak can be conveniently defined as the frequency-dependent spin-freezing temperature $T_f(\nu)$. At the lowest frequency, $T_f(0.1\ \text{Hz}) = 9.0$ K, while at the highest frequency, $T_f(1\ \text{kHz}) = 9.5$ K. The $T_f(\nu)/T_f(0.1\ \text{Hz})$ relation is shown in the inset of Figure 7, yielding the fractional shift of $T_f(\nu)$ per decade of frequency $\Gamma = \Delta T_f/T_f \Delta(\log \nu) = 1.0 \times 10^{-2}$. This value is typical for SGs, where Γ values in the range 10^{-2}−10^{-3} are common.[39]

3.2. Magnetization Versus Magnetic Field Curves

The magnetization versus the magnetic field, $M(H)$, curves were determined at temperatures between 300 and 1.8 K for the field sweep $\mu_0 H = \pm 7$ T and the curves at selected temperatures are shown in Figure 8a. The magnetization M is presented in units of μ_B per one $Fe_{0.214}Ni_{0.214}Ga_{0.572}$ "average atom" of the $Fe_{1.5}Ni_{1.5}Ga_4$ phase. Hysteresis appears below T_f, as shown on an expanded scale in Figure 8b. The coercive field H_c increases monotonously upon cooling (inset in Figure 8b), reaching the value $\mu_0 H_c = 39$ mT at the lowest temperature of 1.8 K. The hysteresis curves close up in a field of about 1.5 T, as typical for an AFM-type hysteresis (the FM-type hysteresis curves typically close up in about 10-times lower field). In the large-field limit, the $M(H)$ curves saturate to an inclined linear line.

The $M(H)$ curve at $T = 5$ K, which is inside the SG phase, but the hysteresis is still small, was theoretically analyzed by assuming a SG-type continuous and symmetric distribution of the exchange coupling constants $P(\mathcal{J})$, shown schematically in the inset in Figure 9.

Within this model, the $M(H)$ curve was fitted with the simplified expression $M = M_0 \mathcal{L}(x) + \mu_0 k H$. The term $M_0 \mathcal{L}(x)$ accounts for the part of the $P(\mathcal{J})$ distribution on the FM ($\mathcal{J} > 0$) side of the $\mathcal{J}$ axis, where $\mathcal{L}(x)$ is the Langevin function with $x = \mu\mu_0 H/(k_B T)$ and $\mu = g\mu_B S$ (where

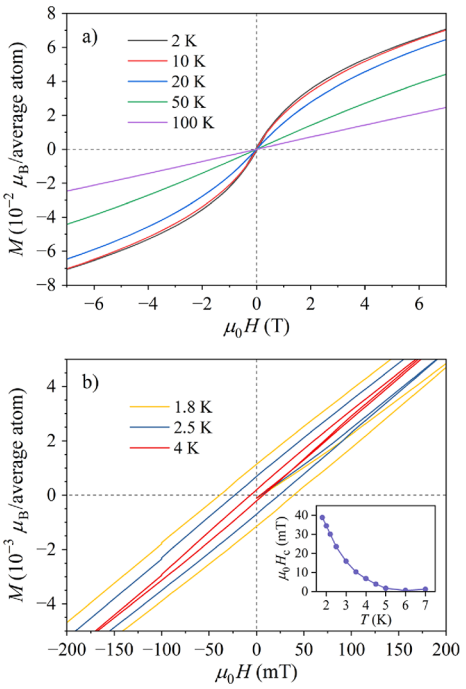

Figure 8. (a) $M(H)$ curves at selected temperatures below and above the spin-freezing temperature $T_f \approx 9$ K. (b) The $M(H)$ curves below T_f expanded around the origin $H = 0$ to show the hysteretic region. The temperature-dependent coercive field H_c is presented in the inset.

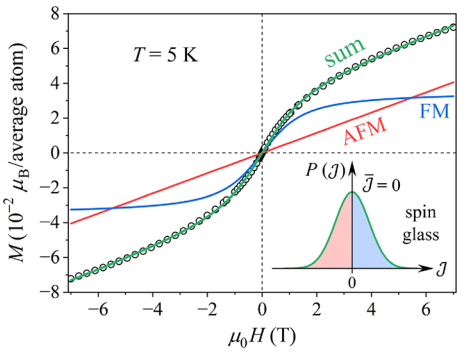

Figure 9. Experimental $M(H)$ curve at $T = 5$ K (open circles) together with the theoretical fit (for details and fit parameter values, see the text). The FM and AFM contributions to the total M are also shown. The spin-glass distribution function of the exchange coupling constants $P(\mathcal{J})$ is shown schematically in the inset.

g denotes the Landé factor and S is the spin). The Langevin model treats the magnetic moment as a classical vector that can assume any value ($S \rightarrow \infty$), accounting for the large effective FM group spins. The Langevin function cannot reproduce the hysteresis, but just the average behavior of the $M(H)$ curve within the hysteretic region. In the large x limit, the $M_0 \mathcal{L}(x)$ term saturates to a horizontal plateau. The term $\mu_0 k H$ accounts for the part of $P(\mathcal{J})$ on the AFM ($\mathcal{J} < 0$) side, where $\mu_0 k$ is the AFM susceptibility. This term is linear in H for any field value. The total $M(H)$ curve therefore grows rapidly at low fields due to the Langevin function, while in the large field limit, it approaches asymptotically an inclined linear line with the slope $\mu_0 k$.

The theoretical fit of the 5 K $M(H)$ curve is presented in Figure 9, showing good agreement with the experimental data and supporting the above SG model with mixed FM−AFM

https://doi.org/10.1021/acs.inorgchem.5c05447
Inorg. Chem. XXXX, XXX, XXX−XXX

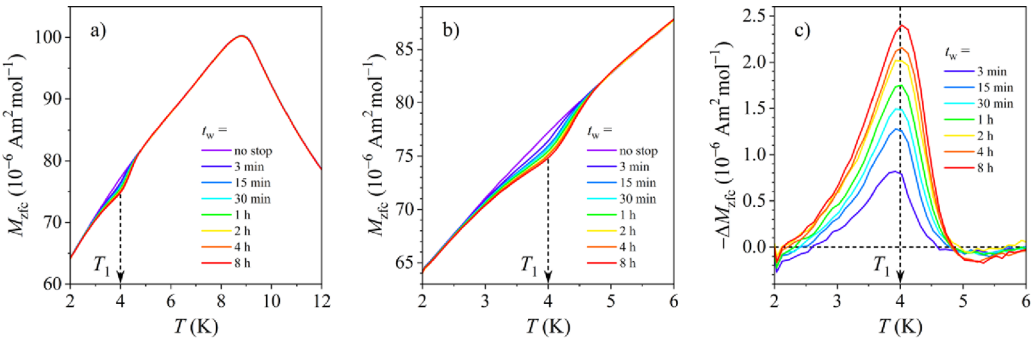

Figure 10. (a) M_{zfc} curves for the aging stop at T_1 = 4 K using different aging times t_w between 3 min and 8 h. (b) Expanded M_{zfc} curves in the region of T_1. (c) Difference ΔM_{zfc} between the reference (unaged) curve and the aged curves (for definition, see the text).

interactions. The FM and AFM contributions to the total fit are also shown separately. The fit-determined parameter values are $M_0 = 3.5 \times 10^{-2}$ μ_B/average atom, $\mu = 12.5$ μ_B and $k = 5.8 \times 10^{-3}$ μ_B/(average atom T).

3.3. Memory Effect

Below the spin-freezing temperature T_f, ergodicity of the magnetically frustrated SG system is broken, because thermal spin fluctuations become too slow to drive the spin system into thermal equilibrium within the observation time window of the experimental technique. The nonergodic spin system is out of equilibrium and the observable physical quantities become time-dependent instead of being time-independent thermodynamic quantities. On the experimental time scale, the spin system slowly approaches thermal equilibrium, but cannot reach it because it does not have enough time to explore the entire phase space.

A spectacular manifestation of the out-of-equilibrium dynamics of a nonergodic spin system is the memory effect (ME).[35,40−53] In the ME experiment, the spin system is continuously cooled in zero magnetic field from the paramagnetic (ergodic) phase through T_f into the nonergodic SG phase. At a certain temperature $T_1 < T_f$, isothermal aging of the spin system is performed by stopping the cooling for a waiting (aging) time t_w that ranges from minutes to hours. After t_w, the cooling is resumed and eventually one or more additional aging stops are performed at lower temperatures $T_i < T_1$. At the lowest temperature, a tiny magnetic field of the order 0.1 mT is applied, the cooling is reversed to heating and the zfc magnetization M_{zfc} is measured in a continuous heating run. The ME is manifested in the M_{zfc}, which shows a diminution (a dip) at all stop temperatures T_i relative to the M_{zfc} for the no-stop case (no aging at any temperature), and the diminution is deeper for longer t_w. The out-of-equilibrium spin system remembers all aging stops during cooling and also the duration t_w of each stop. By heating above T_f into the ergodic phase, all the memorized information is erased and the spin system is "rejuvenated", i.e., it is the same as before aging.

The ME in the $Fe_{1.5}Ni_{1.5}Ga_4$ intermetallic compound was investigated by performing the aging stop at T_1= 4 K and employing a set of seven approximately logarithmically spaced aging times t_w between 3 min and 8 h, where each t_w was used in a separate experiment. A no-stop ($t_w = 0$) reference run was also conducted. After t_w, the cooling has resumed to the lowest temperature of 1.8 K, where the magnetic field $\mu_0 H$ = 0.5 mT was switched on and M_{zfc} was recorded in a heating run. The M_{zfc} s of all experiments with different t_w s are shown superimposed in Figure 10a, where it is observed that the aged M_{zfc} curves exhibit a dip at the aging temperature T_1 = 4 K relative to the reference one.

The expanded M_{zfc} curves around 4 K are shown in Figure 10b, where the monotonous increase of the dip with increasing t_w can be seen in more detail. In Figure 10c, the difference between the reference $M_{zfc}(t_w = 0)$ and the aged M_{zfc} s, $\Delta M_{zfc} = M_{zfc}(t_w) - M_{zfc}(t_w = 0)$, is shown, where it is evident that ΔM_{zfc} appears in the form of a resonant curve peaked at the aging temperature 4 K and its magnitude increases with t_w.

In the second set of experiments, the temperature dependence of ME was investigated by conducting the above-described single-stop experiment at a set of aging temperatures T_1 between 9 and 3 K with the interval ΔT_1 = 1 K, and in addition at 2.5 K. The aging time t_w = 1 h was employed in each experiment. The M_{zfc} s for all aging temperatures, together with the reference $M_{zfc}(t_w = 0)$ are shown superimposed in Figure 11a. At each aging temperature T_1 (except at $T_1 = T_f$ = 9 K), the $M_{zfc}(t_w$ = 1 h) shows a diminution with respect to the reference $M_{zfc}(t_w = 0)$, where the diminution is peaked at T_1.

In Figure 11b, the differences ΔM_{zfc} for all aging temperatures are shown superimposed, demonstrating the presence of ME at any temperature below the spin freezing temperature T_f, and confirming broken ergodicity of the SG state on the experimental time scale.

4. DISCUSSION

As already discussed, the too similar X-ray atomic scattering factors and too close neutron coherent scattering lengths of the Fe and Ni prevent the XRD and neutron diffraction techniques to distinguish between two possible structural models of the $Fe_{1.5}Ni_{1.5}Ga_4$ phase, the cubic $Ia\bar{3}d$ model with statistical distribution of the Fe and Ni atoms at their Wyckoff site and the symmetry-reduced chiral model $I4_132$ with chemical ordering of Fe and Ni. The observation of the low-temperature SG phase is, however, in favor of the disordered cubic $Ia\bar{3}d$ model via the following arguments. SGs are by definition site-disordered spin systems that conform to two basic criteria: (1) randomness (the magnetic moments of either single type or different types are positioned randomly in the crystal lattice) and (2) frustration (no moments' configuration can satisfy all the bonds and minimize the energy at the same time).[35] These two properties make the free-energy landscape of a SG highly structured, comprising many degenerate or nearly degenerate metastable states separated by a distribution of energy barriers. To reach the thermal-equilibrium collective spin state, the spins must explore the complete phase space by surmounting the barriers via thermally activated overbarrier jumps or by

https://doi.org/10.1021/acs.inorgchem.5c05447
Inorg. Chem. XXXX, XXX, XXX−XXX

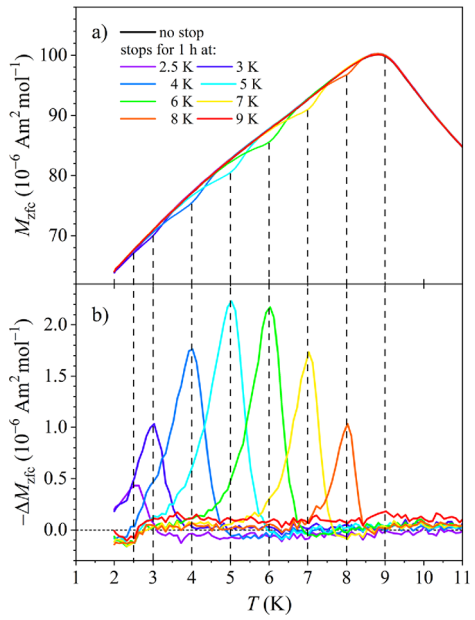

Figure 11. (a) M_{zfc} s of the single-stop experiments for the aging temperatures T_1 between 9 and 3 K in steps of ΔT_1 = 1 K, and in addition at 2.5 K, superimposed on the same graph. The aging time t_w = 1 h was employed in all experiments. The no-stop reference $M_{zfc}(t_w = 0)$ is also shown. (b) The difference ΔM_{zfc} between the no-stop reference magnetization and the aged magnetization for each aging temperature.

quantum tunneling through the barriers. The small thermal energy k_BT at low temperatures and the broad distribution of barriers between metastable states prevent the spin system to reach thermal equilibrium on the accessible experimental time scale, resulting in broken ergodicity below the spin-freezing temperature T_f. The presented magnetic experiments clearly demonstrate that the Fe and Ni magnetic moments in the $Fe_{1.5}Ni_{1.5}Ga_4$ are in a SG configuration, supporting their random distribution at the 48*g* Wyckoff site in the unit cell, which is compatible with the $Ia\bar{3}d$ chemically disordered structural model. Chemical ordering of the Fe and Ni atoms would result in a periodic distribution of the Fe and Ni moments on two magnetic sublattices, promoting the formation of a single periodic magnetic structure (such as FM or AFM or ferrimagnetic) without randomness. Since this has not been observed experimentally, the symmetry-reduced chiral structural model $I4_132$ of the $Fe_{1.5}Ni_{1.5}Ga_4$ phase with chemically ordered Fe and Ni is unlikely.

The memory effect in frustrated spin systems is still incompletely understood, because theoretical simulations of this out-of-equilibrium phenomenon are hampered by the nonthermodynamic nature of the involved physical quantities, i.e. by the fact that the quantities depend on the observation-time window instead of being time-independent thermodynamic quantities (the latter are obtained when the observation time window is much longer than the correlation times of the thermal fluctuations). A comprehensive literature on the ME in frustrated spin systems is available,[35,40−53] and the interested reader is referred to those articles. In the context of this study, the purpose of presenting the ME was not to add general understanding of this spectacular phenomenon, but to help distinguish between the two possible structural models of the $Fe_{1.5}Ni_{1.5}Ga_4$ phase, where the observation of the ME favors the $Ia\bar{3}d$ model.

5. CONCLUSIONS

In this work, the Ga-rich region of the Fe−Ni−Ga ternary phase diagram was investigated, by exploring a line of compositions at a constant Ga content $Fe_xNi_{3-x}Ga_4$, with $0.5 \leq x \leq 2.5$. Single-phase material was found only at the composition $Fe_{1.5}Ni_{1.5}Ga_4$ and its immediate vicinity, representing a new phase in the Fe−Ni−Ga ternary system. The homogeneity range of the $Fe_{1.5}Ni_{1.5}Ga_4$ phase was estimated by additionally exploring a set of compositions $Fe_xNi_yGa_z$, where the concentrations of all three elements were varied independently around the central composition $Fe_{1.5}Ni_{1.5}Ga_4$. The structural model of the $Fe_{1.5}Ni_{1.5}Ga_4$ phase was constructed based on the structure of the binary Ni_3Ga_4 parent phase, which crystallizes in the cubic $Ia\bar{3}d$ space group. Despite having substantial distortions in the unit cell, we have considered that by substituting Fe for Ni, the parent cubic $Ia\bar{3}d$ structure is preserved in the $Fe_{1.5}Ni_{1.5}Ga_4$, where Fe and Ni are statistically distributed at the 48*g* Wyckoff site in the unit cell. However, the possibility of a symmetry-reduced chiral structural model $I4_132$, driven by chemical ordering between Fe and Ni cannot be entirely ruled out on the basis of the crystallographic study performed by XRD and neutron diffraction techniques, because of insufficient X-ray scattering contrast and minimal difference in the neutron coherent scattering lengths of Fe and Ni. Magnetic properties of the $Fe_{1.5}Ni_{1.5}Ga_4$ phase were investigated as well, finding that the material forms a spin glass phase below the spin freezing temperature $T_f \approx 9$ K. Since the spin glass-type magnetic ordering of the Fe and Ni magnetic moments is compatible with their random distribution at the particular Wyckoff site in the unit cell, the magnetic study supports the disordered cubic $Ia\bar{3}d$ structural model of the $Fe_{1.5}Ni_{1.5}Ga_4$ phase, without chemical ordering of the Fe and Ni.

6. EXPERIMENTAL SECTION

6.1. Single-Crystal X-ray Diffraction Data Collection and Processing

Properly shaped crystals with desired compositions were selected for the SCXRD studies. The crystals were mounted on the goniometer head using a noncrystalline adhesive. The diffraction intensities were collected by Bruker Photon II detector equipped with a monochromatic Mo Kα radiation (λ = 0.71073 Å) using Bruker D8 Quest instrument. Data was acquired with a scan width of 1° and an exposure time of 3−4 s, maintaining the sample-to-detector distance of 50 mm. Apex4 software[54] was used for the data collection, reduction and integration. The precession image was generated by employing CrysAlisPro software.[55] The charge flipping algorithm was used for the structure solution, implemented in Superflip[31] embedded in the JANA2006 software.[32] The refinement was performed using the same software.

6.2. EDS Analysis

Energy dispersive X-ray spectroscopy analysis of the chemical composition was performed by the scanning electron microscope ThermoFisher Verios 4G HP equipped with EDS Oxford Instruments AZtec Live, Ultim Max SDD 65 mm^2 detection system.

6.3. Neutron Powder Diffraction Data Collection

Neutron powder diffraction data were collected on the Echidna high-resolution powder diffractometer with a neutron wavelength of 1.622 Å. The measurements were performed at temperatures 300 and 3 K, using ~2 g of powder sample in a 6 mm-diameter cylindrical vanadium can.

https://doi.org/10.1021/acs.inorgchem.5c05447
Inorg. Chem. XXXX, XXX, XXX−XXX

6.4. Powder X-ray Diffraction Data Collection and Refinement

The phase analyses were performed using PXRD experiment. A portion of the ingot was ground into fine powder using a mortar and pestle. The samples were placed into a zero-background holder, ensuring flat upper surface for optimal data acquisition. Bruker D8 ADVANCE diffractometer with Cu Kα radiation (λ = 1.5418 Å) was used for the PXRD data collection in reflection mode for the 2θ range 10−80° with a scan speed of 2°/min and exposure time of 0.5 s per step. The diffraction data analyses were performed either by the Rietveld method (refining the unit cell based on the positions of the reflections, while their intensities are bound by the structure factors and a refined scale factor) or by the Le Bail method (refining the unit cell based on the positions of the reflections and adjusting the intensities individually to fit best) using the JANA2006 software.[32]

6.5. Magnetic Measurements

Magnetic experiments were conducted on a Quantum Design MPMS3 magnetometer, equipped with a 7 T superconducting magnet and operating at temperatures between 1.8 and 400 K. Low-field experiments were conducted using a copper AC/ULF coil of the MPMS3 magnetometer to ensure an accurate and repeatable magnetic field.

■ ASSOCIATED CONTENT

Supporting Information

The Supporting Information is available free of charge at https://pubs.acs.org/doi/10.1021/acs.inorgchem.5c05447.

Reciprocal space reconstruction images, EDS elemental maps & BSE image, PXRD refinement diffractograms and associated refinement parameters (PDF)

Accession Codes

Deposition Number 2502085 contains the supplementary crystallographic data for this paper. These data can be obtained free of charge via the joint Cambridge Crystallographic Data Centre (CCDC) and Fachinformationszentrum Karlsruhe Access Structures service.

■ AUTHOR INFORMATION

Corresponding Authors

Partha Pratim Jana − *Department of Chemistry, Indian Institute of Technology, Kharagpur 721302, India;* orcid.org/0000-0002-1348-4150; Email: ppj@chem.iitkgp.ac.in

Janez Dolinšek − *Jožef Stefan Institute, SI-1000 Ljubljana, Slovenia; University of Ljubljana, Faculty of Mathematics and Physics, SI-1000 Ljubljana, Slovenia;* orcid.org/0000-0002-5750-802X; Email: janez.dolinsek@ijs.si

Authors

Krishnendu Buxi − *Department of Chemistry, Indian Institute of Technology, Kharagpur 721302, India;* orcid.org/0000-0002-0909-0052

Rahul Pan − *Department of Chemistry, Indian Institute of Technology, Kharagpur 721302, India;* orcid.org/0009-0004-7791-0202

Zvonko Jagličić − *Institute of Mathematics, Physics and Mechanics & University of Ljubljana, Faculty of Civil and Geodetic Engineering, SI-1000 Ljubljana, Slovenia*

Andreja Jelen − *Jožef Stefan Institute, SI-1000 Ljubljana, Slovenia*

Jože Luzar − *Jožef Stefan Institute, SI-1000 Ljubljana, Slovenia*

Peter Mihor − *Jožef Stefan Institute, SI-1000 Ljubljana, Slovenia*

Stanislav Vrtnik − *Jožef Stefan Institute, SI-1000 Ljubljana, Slovenia; University of Ljubljana, Faculty of Mathematics and Physics, SI-1000 Ljubljana, Slovenia*

Primož Koželj − *Jožef Stefan Institute, SI-1000 Ljubljana, Slovenia; University of Ljubljana, Faculty of Mathematics and Physics, SI-1000 Ljubljana, Slovenia;* orcid.org/0000-0001-9837-7516

Julia Petrović − *Jožef Stefan Institute, SI-1000 Ljubljana, Slovenia*

Maxim Avdeev − *Australian Nuclear Science and Technology Organisation, Lucas Heights, NSW 2234, Australia; School of Chemistry, The University of Sydney, Sydney, NSW 2006, Australia;* orcid.org/0000-0003-2366-5809

Complete contact information is available at: https://pubs.acs.org/10.1021/acs.inorgchem.5c05447

Author Contributions

The manuscript was written through contributions of all authors. All authors have given approval to the final version of the manuscript.

Notes

No uncommon hazards are noted.
The authors declare no competing financial interest.

■ ACKNOWLEDGMENTS

P.P.J. would like to thank the Anusandhan National Research Foundation (ANRF), India (grant No. CRG/2020/004115), for financial support. K.B. acknowledges IIT Kharagpur for his research fellowship. R.P. acknowledges the Prime Minister Research Fellowship (PMRF) for his research fellowship. The Slovenian authors acknowledge the financial support from the Slovenian Research and Innovation Agency (Research Core Fundings No. P1-0125 and No. P2-0348 and Project No. N1-0330).

■ REFERENCES

(1) Heletta, L.; Block, T.; Klenner, S.; Pöttgen, R. Ternary transition metal gallides with TiNiSi, ZrBeSi and $MgZn_2$-type structure. *Z. Naturforsch. B* **2019**, *74*, 297−306.

(2) Lukacheva, S. M.; Zakharova, E. Yu.; Makhaneva, A. Yu.; Nesterenko, S. N.; Kazakov, S. M.; Lyssenko, K. A.; Banaru, A. M.; Kuznetsov, A. N. One nickel too many: a distorted $HoCoGa_5$-type structure motif and topological heteroclusters in a ternary $Ti_{2-x}Ni_3Ga_9$ intermetallic. *J. Solid State Chem.* **2025**, *345*, No. 125223.

(3) Buschow, K. H. J.; van Engen, P. G. Magnetic and magneto-optical properties of heusler alloys based on aluminium and gallium. *J. Magn. Magn. Mater.* **1981**, *25*, 90−96.

(4) Xie, W.; Luo, H.; Phelan, B. F.; Klimczuk, T.; Cevallos, F. A.; Cava, R. J. Endohedral gallide cluster superconductors and superconductivity in $ReGa_5$. *Proc. Natl. Acad. Sci. U. S. A.* **2015**, *112*, E7048−E7054.

(5) Khalaniya, R. A.; Verchenko, V. Yu.; Zonov, E. M.; Stern, R.; Shevelkov, A. V. Crystal structure, chemical bonding, and magnetism of α-Fe_6Ga_5: How local interactions shape the structure and properties of intermetallic compounds. *Inorg. Chem.* **2024**, *63*, 21099−21109.

(6) Gourdon, O.; Miller, G. J. Reinvestigation of the GaMn structure and theoretical studies of its electronic and magnetic properties. *J. Solid State Chem.* **2003**, *173*, 137−147.

(7) Kerrai, H.; Saadi, H.; Jalal, E. M.; Kerouad, M.; Zaim, A. Hysteresis behavior and magnetocaloric effect in $MnNiGa_2$ full-Heusler alloy. *Solid State Commun.* **2024**, *394*, No. 115717.

https://doi.org/10.1021/acs.inorgchem.5c05447
Inorg. Chem. XXXX, XXX, XXX−XXX

(8) Tiwari, N.; Pal, V.; Das, S.; Paliwal, M. Proposed compositions in a Ni−Mn−Ga system for magnetocaloric applications. *J. Electron. Mater.* **2024**, *53*, 1773−1795.
(9) Sokolovskiy, V. V.; Sokolovskaya, Yu. A.; Zagrebin, M. A.; Buchelnikov, V. D.; Zayak, A. T. Ternary diagrams and magnetic properties of Ni−Mn−Ga Heusler alloys from *ab initio* and Monte Carlo studies. *J. Magn. Magn. Mater.* **2019**, *470*, 64−68.
(10) Miroshkina, O. N.; Sokolovskiy, V. V.; Zagrebin, M. A.; Taskaev, S. V.; Buchelnikov, V. D. Theoretical approach to investigation of the magnetic and magnetocaloric properties of Heusler Ni−Mn−Ga alloys. *Phys. Solid State* **2020**, *62*, 785−792.
(11) Sokolovskaya, Yu.; Miroshkina, O.; Baigutlin, D.; Sokolovskiy, V.; Zagrebin, M.; Buchelnikov, V.; Zayak, A. T. A ternary map of Ni−Mn−Ga Heusler alloys from *ab initio* calculations. *Metals* **2021**, *11*, 973.
(12) Saito, T.; Watanabe, H. Magnetic and thermoelectric properties of Fe_2CoGa Heusler compounds. *Inorganics* **2025**, *13*, 33.
(13) Osswald, J.; Giedigkeit, R.; Jentoft, R. E.; Armbrüster, M.; Girgsdies, F.; Kovnir, K.; Grin, Yu.; Schlögl, R.; Ressler, T. Palladium−gallium intermetallic compounds for the selective hydrogenation of acetylene: Part I: Preparation and structural investigation under reaction conditions. *J. Catal.* **2008**, *258*, 210−218.
(14) Osswald, J.; Kovnir, K.; Armbrüster, M.; Giedigkeit, R.; Jentoft, R. E.; Wild, U.; Grin, Yu.; Schlögl, R. Palladium−gallium intermetallic compounds for the selective hydrogenation of acetylene: Part II: Surface characterization and catalytic performance. *J. Catal.* **2008**, *258*, 219−227.
(15) Armbrüster, M.; Kovnir, K.; Behrens, M.; Teschner, D.; Grin, Yu.; Schlögl, R. Pd−Ga intermetallic compounds as highly selective semihydrogenation catalysts. *J. Am. Chem. Soc.* **2010**, *132*, 14745−14747.
(16) Ota, A.; Armbrüster, M.; Behrens, M.; Rosenthal, D.; Friedrich, M.; Kasatkin, I.; Girgsdies, F.; Zhang, W.; Wagner, R.; Schlögl, R. Intermetallic compound Pd_2Ga as a selective catalyst for the semihydrogenation of acetylene: From model to high performance systems. *J. Phys. Chem. C* **2011**, *115*, 1368−1374.
(17) Studt, F.; Sharafutdinov, I.; Abild-Pedersen, F.; Elkjær, C. F.; Hummelshøj, J. S.; Dahl, S.; Chorkendorff, I.; Nørskov, J. K. Discovery of a Ni−Ga catalyst for carbon dioxide reduction to methanol. *Nat. Chem.* **2014**, *6*, 320−324.
(18) Sharafutdinov, I.; Elkjær, C. F.; Pereira de Carvalho, H. W.; Gardini, D.; Chiarello, G. L.; Damsgaard, C. D.; Wagner, J. B.; Grunwaldt, J. D.; Dahl, S.; Chorkendorff, I. Intermetallic compounds of Ni and Ga as catalysts for the synthesis of methanol. *J. Catal.* **2014**, *320*, 77−88.
(19) Wencka, M.; Kovač, J.; Dasireddy, V. D. B. C.; Likozar, B.; Jelen, A.; Vrtnik, S.; Gille, P.; Kim, H. J.; Dolinšek, J. The effect of surface oxidation on the catalytic properties of Ga_3Ni_2 intermetallic compound for carbon dioxide reduction. *J. Anal. Sci. Technol.* **2018**, *9*, 12.
(20) Singh, A. K.; Wang, W.; Panda, D. P.; Bagchi, D.; Goud, D.; Ray, B.; He, J.; Peter, S. C. Cobalt-induced phase transformation of Ni_3Ga_4 generates chiral intermetallic $Co_3Ni_3Ga_8$. *J. Am. Chem. Soc.* **2023**, *145*, 1433−1440.
(21) Ellner, M.; Kek, S.; Predel, B. Ni_3Al_4 − A phase with ordered vacancies isotypic to Ni_3Ga_4. *J. Less Common Met.* **1989**, *154*, 207−215.
(22) Ellner, M.; Best, K. J.; Jacobi, H.; Schubert, K. Struktur von Ni_3Ga_4. *J. Less Common Met.* **1969**, *19*, 294−296.
(23) Raghavan, V. Fe−Ga−Ni (Iron−Gallium−Nickel). *J. Phase Equilib. Diffus.* **2009**, *30*, 98−99.
(24) Zhang, Y. J.; Wang, W. H.; Zhang, H. G.; Liu, E. K.; Ma, R. S.; Wu, G. H. Structure and magnetic properties of Fe_2NiZ (Z= Al, Ga, Si and Ge) Heusler alloys. *Physica B* **2013**, *420*, 86−89.
(25) Lu, J. B.; Yang, H. X.; Tian, H. F.; Zeng, L. J.; Ma, C.; Feng, L.; Wu, G. H.; Li, J. Q.; Jansen, J. Cooperative effect of monoclinic distortion and sinusoidal modulation in the martensitic structure of Ni2FeGa. *J. Solid State Chem.* **2010**, *183*, 425−430.
(26) Oikawa, K.; Ota, T.; Ohmori, T.; Tanaka, Y.; Morito, H.; Fujita, A.; Kainuma, R.; Fukamichi, K.; Ishida, K. Magnetic and martensitic phase transitions in ferromagnetic Ni−Ga−Fe shape memory alloys. *Appl. Phys. Lett.* **2002**, *81*, 5201−5203.
(27) Philippe, M. J.; Malaman, B.; Roques, B.; Courtois, A.; Protas, J. Structures cristallines des phases Fe3Ga4 et Cr3Ga4. *Acta Crystallogr.* **1975**, *B31*, 477−482.
(28) Kawamiya, N.; Adachi, K. Magnetic and Mössbauer studies of metamagnetic Fe3Ga4. *J. Phys. Soc. Jpn.* **1986**, *55*, 634−640.
(29) Dasarathy, C.; Hume-Rothery, W. The system iron-gallium. *Proc. R. Soc. London A* **1965**, *286*, 141−157.
(30) Al-Kanani, H. J.; Booth, J. G.; Ko, K. Y. Magnetic phase transitions in $(Fe_{1-x}T_x)_3Ga_4$ alloys. *J. Appl. Phys.* **2000**, *87*, 4879−4881.
(31) Palatinus, L.; Chapuis, G. SUPERFLIP − a computer program for the solution of crystal structures by charge flipping in arbitrary dimensions. *J. Appl. Crystallogr.* **2007**, *40*, 786−790.
(32) Petříček, V.; Dušek, M.; Palatinus, L. Crystallographic computing system JANA2006: General features. *Z. Kristallogr.—Cryst. Mater.* **2014**, *229*, 345−352.
(33) Hempelmann, R. *Quasielastic Neutron Scattering and Solid State Diffusion (Oxford Series on Neutron Scattering in Condensed Matter)*; Oxford Academic: Oxford, U.K., 2000; pp 26−53 (Ch. 3).
(34) Yannello, V. J.; Fredrickson, D. C. Generality of the 18-*n* rule: Intermetallic structural chemistry explained through isolobal analogies to transition metal complexes. *Inorg. Chem.* **2015**, *54*, 11385−11398.
(35) Binder, K.; Young, A. P. Spin glasses: Experimental facts, theoretical concepts, and open questions. *Rev. Mod. Phys.* **1986**, *58*, 801−976.
(36) Mabbs, F. E.; Machin, D. J. *Magnetism and Transition Metal Complexes*; Chapman and Hall: London, U.K., 1973; p 7.
(37) Bain, G. A.; Berry, J. F. Diamagnetic corrections and Pascal's constants. *J. Chem. Educ.* **2008**, *85*, 532−536.
(38) Coey, J. M. D. *Magnetism and Magnetic Materials*; Cambridge University Press: Cambridge, U.K., 2010; p 216.
(39) Mydosh, J. A. *Spin Glasses: An Experimental Introduction*; Taylor & Francis: London, U.K., 1993; p 67.
(40) Bouchaud, J.-P.; Cugliandolo, L. F.; Kurchan, J.; Mézard, M. *Spin Glasses and Random Fields*; Young, A. P., Ed.; World Scientific: Singapore, 1998; pp 161−224.
(41) Vincent, E.; Hammann, J.; Ocio, M.; Bouchaud, J.-P.; Cugliandolo, L. F. *Complex Behaviour of Glassy Systems*; Rubi, M., Ed.; Springer-Verlag: Berlin, Germany, 1997; *Vol. 492*, pp 184−219.
(42) Nordblad, P.; Svedlindh, P. *Spin Glasses and Random Fields*; Young, A. P., Ed.; World Scientific: Singapore, 1998; pp 1−28.
(43) Bouchaud, J.-P.; Dupuis, V.; Hammann, J.; Vincent, E. Separation of time and length scales in spin glasses: Temperature as a microscope. *Phys. Rev. B* **2001**, *65*, No. 024439.
(44) Lederman, M.; Orbach, R.; Hammann, J. M.; Ocio, M.; Vincent, E. Dynamics in spin glasses. *Phys. Rev. B* **1991**, *44*, 7403−7412.
(45) Chu, D.; Kenning, G. G.; Orbach, R. Effect of magnetic fields on the relaxation of the thermoremanent magnetization in spin glasses. *Philos. Mag. B* **1995**, *71*, 479−488.
(46) Refregier, Ph.; Vincent, E.; Hammann, J.; Ocio, M. Ageing phenomena in a spin-glass: effect of temperature changes below T_g. *J. Phys. (Paris)* **1987**, *48*, 1533−1539.
(47) Dolinšek, J.; Jagličić, Z.; Sato, T. J.; Guo, J. Q.; Tsai, A. P. Spin freezing in icosahedral Tb−Mg−Zn and Tb−Mg−Cd quasicrystals. *J. Phys.: Condens. Matter* **2003**, *15*, 7981−7996.
(48) Dolinšek, J.; Slanovec, J.; Jagličić, Z.; Heggen, M.; Balanetskyy, S.; Feuerbacher, M.; Urban, K. Broken ergodicity, memory effect, and rejuvenation in Taylor-phase and decagonal Al_3(Mn,Pd,Fe) complex intermetallics. *Phys. Rev. B* **2008**, *77*, No. 064430.
(49) Jonason, K.; Vincent, E.; Hammann, J.; Bouchaud, J. P.; Nordblad, P. Memory and chaos effects in spin glasses. *Phys. Rev. Lett.* **1998**, *81*, 3243−3246.

https://doi.org/10.1021/acs.inorgchem.5c05447
Inorg. Chem. XXXX, XXX, XXX−XXX

(50) Dupuis, V.; Vincent, E.; Bouchaud, J. P.; Hammann, J.; Ito, A.; Katori, H. A. Aging, rejuvenation, and memory effects in Ising and Heisenberg spin glasses. *Phys. Rev. B* **2001**, *64*, No. 174204.
(51) Dolinšek, J.; Feuerbacher, M.; Jagodič, M.; Jagličić, Z.; Heggen, M.; Urban, K. A Thermal Memory Cell. *J. Appl. Phys.* **2009**, *106*, No. 043917.
(52) Ghanta, S.; Das, A.; Jana, P. P.; Vrtnik, S.; Gačnik, D.; Luzar, J.; Jelen, A.; Koželj, P.; Wencka, M.; Dolinšek, J. Structure and spin-glass magnetism of the $Mn_xNi_2Zn_{11-x}$ pseudo-binary γ-brasses at low Mn contents. *Inorg. Chem.* **2021**, *60*, 12226−12236.
(53) Mondal, A.; Dey, R.; Jelen, A.; Koželj, P.; Kuila, S. K.; Pan, R.; Vrtnik, S.; Luzar, J.; Wencka, M.; Petrović, J.; Mihor, P.; Jagličić, Z.; Meden, A.; Jana, P. P.; Dolinšek, J. Double helix of icosahedra structure and spin glass magnetism of the δ-$Co_{2.5}Zn_{17.5-x}Mn_x$ (x = 0.4−3.5) pseudo-binary alloys. *Inorg. Chem.* **2024**, *63*, 10251−10263.
(54) Bruker (**2001**). Bruker AXS Inc.: Madison, Wisconsin, USA.
(55) Rigaku Oxford Diffraction, 2018. *CrysAlisPro Software system*; Rigaku Corporation: Oxford, U.K..

https://doi.org/10.1021/acs.inorgchem.5c05447
Inorg. Chem. XXXX, XXX, XXX−XXX